Analysis of near-infrared spectroscopy and indocyanine green dye dilution with Monte Carlo simulation of light propagation in the adult brain

R. Mudra
A. Nadler
Institute of Biomedical Engineering
University and ETH Zürich
Gloriastrasse 35
8092 Zürich, Switzerland
E-mail: mudra@biomed.ee.ethz.ch

E. Keller
University Hospital of Zürich
Department of Neurosurgery
8092 Zürich, Switzerland

P. Niederer
Institute of Biomedical Engineering
University and ETH Zürich
Gloriastrasse 35
8092 Zürich, Switzerland

Abstract. Near-infrared spectroscopy (NIRS) combined with indocyanine green (ICG) dilution is applied externally on the head to determine the cerebral hemodynamics of neurointensive care patients. We applied Monte Carlo simulation for the analysis of a number of problems associated with this method. First, the contamination of the optical density (OD) signal due to the extracerebral tissue was assessed. Second, the measured OD signal depends essentially on the relative blood content (with respect to its absorption) in the various transilluminated tissues. To take this into account, we weighted the calculated densities of the photon distribution under baseline conditions within the different tissues with the changes and aberration of the relative blood volumes that are typically observed under healthy and pathologic conditions. Third, in case of NIRS ICG dye dilution, an ICG bolus replaces part of the blood such that a transient change of absorption in the brain tissues occurs that can be recorded in the OD signal. Our results indicate that for an exchange fraction of $\Delta = 30\%$ of the relative blood volume within the intracerebral tissue, the OD signal is determined from 64 to 74% by the gray matter and between 8 to 16% by the white matter maximally for a distance of $d = 4.5$ cm.
© 2006 Society of Photo-Optical Instrumentation Engineers. [DOI: 10.1117/1.2341652]

Keywords: near-infrared; spectroscopy; absorption; scattering; lasers in medicine.

Paper 04217RRRR received Nov. 10, 2005; revised manuscript received Apr. 25, 2006; accepted for publication Apr. 25, 2006; published online Sep. 6, 2006.

1 Introduction

In 1977, near-infrared spectroscopy (NIRS) was used for the first time as a noninvasive measurement method to detect changes in the cerebral hemoglobin oxygenation (oxy-Hb, Deoxy-Hb).[1] More recently, NIRS has been applied to estimate cerebral oxygenation under routine clinical conditions.[2,3] Furthermore, for an improved monitoring of cerebral hemodynamics in neurointensive care, NIRS has been combined with indocyanine green (ICG) dye bolus injection,[4] whereby ICG is a highly absorbing tracer substance in the IR region. This procedure allows us to determine the mean transit time of ICG (mtt_{ICG}), the cerebral blood volume (CBV), and the cerebral blood flow (CBF) of adult patients at the bedside.[5,6] The technique has recently been validated in healthy volunteers.[6]

Early detection and treatment of cerebral ischemia to prevent further neurological damage in patients with severe brain injury and stroke is one of the most important issues in neurocritical care. Patients in the neurointensive care unit are mostly in a critical, unstable condition. Stable xenon-enhanced computed tomography, positron emission tomography, single-photon emission computed tomography, or magnetic resonance spectroscopy are powerful research tools,[7–10] but they require the patient to be transported and thus involve a potentially high risk. The established methods for bedside measurement of CBF with inert tracers such as the nitrous oxide dilution method[11] or the 133Xenon dilution technique[12] are difficult to perform clinically and are time-consuming. Additionally, 133Xenon dilution detected with multiple collimators measures regional cortical perfusion, which may not be representative when cortical electrical depression is present.[13]

The NIRS method does not involve spectroscopy in the strict sense, but is restricted to an intensity measurement of the transmitted light at different wavelengths; whereby for each wavelength, the transmitted light has the same wavelength as the incident light. A distinction thereby has to be made between a baseline signal, which for all practical purposes is constant in time and depends, among other things, strongly on the relative blood content of the involved tissues, and a time-dependent signal, which is caused by a number of effects, such as a variation of the blood oxygenation, the passage of a tracer, or a short-term change of the relative blood volume contained in the blood vessels in the various tissues involved in the photon paths. Because the baseline is usually not of interest clinically, the time varying signal is extracted with the aid of a difference procedure such that the baseline

Address all correspondence to Regina Mudra, Institute of Biomedical Engineering, Gloriastrasse 35 Zürich, Switzerland CH-8092 Zürich Switzerland; Tel: 41 44 632 45 95; Fax: 41 44 632 11 93; E-mail: mudra@biomed.ee.ethz.ch

1083-3668/2006/11(4)/044009/14/$22.00 © 2006 SPIE

drops out. This signal is normalized and denoted as the optical density (OD) signal. Along with the baseline, however, the OD signal depends largely on the relative tissue blood content because the time dependency is due mostly to variations taking place in the intravascular space.

A problem associated with the NIRS ICG dye dilution method used for CBF measurement is due to the fact that the OD signal from the brain tissue is contaminated by contributions from the extracerebral bone and scalp tissue. From a clinical point of view, the spatial photon density distribution, that is, the spatial sensitivity profile that characterizes the volume interrogated by NIRS between emitter and receiver,[14] should be concentrated in the brain tissues of interest with minimal contamination by other structures. Accordingly, several theoretical and experimental approaches were made to analyze the influence of these contaminations on the measured OD signal.[15–19] Among others, these investigations supported the finding that the cerebrospinal fluid (CSF) in the subarachnoid acts as a light guide.[20]

One method to subtract the extracerebral contamination from the detected OD signal is based on spatially resolved spectroscopy (SRS).[21] The localization of the origin of the various contributions to the measured OD signal is thereby derived from consecutive NIRS measurements with different emitter-detector spacings. However, interindividual variability of anatomy restricts the applicability of SRS, mostly because individual verification and calibration is unsuitable for rapid noninvasive CBF measurements at the bedside, in particular in the neurointensive care unit. Other methods are based on time-resolved spectroscopy (TRS)[22,23] or high frequency modulated[24] measurements.

As Monte Carlo (MC) methods lend themselves for the analysis of light propagation in biological tissues, a number of studies relating to the application of NIRS in the brain have been presented.[25–28] Most simulations were thereby performed on homogeneous geometrical structures[14,29] not taking into account the different tissues the light has to pass through nor the folded surface structure of the brain. Such approaches suffer in reality, because they do not reflect the scattering differences in the various tissues and geometries. Other approaches were based on two-dimensional (2D) magnetic resonance images (MRI) to separate the different tissues, such as the scalp, skull, and CSF layer.[30,31] Recently, also three-dimensional (3D) head models derived from MRI data were used to simulate the light propagation in the head.[32,33]

In this paper, results from MC simulations are presented where light propagation, more precisely, the propagation of photons, was simulated between an emitter and a detector externally attached to the adult head. For these simulations, a 3D anatomical brain model was obtained from MRI data of a healthy, 30-year-old male volunteer. The implementation of the MC code followed the theoretical description of Prahl,[34] a significant difference being the application of a fixed sufficiently small step-size for the photon propagation such that anatomical details could be taken into account. From the simulation, the contribution of the various tissues to the total absorption is obtained which in all cases considered allowed us to assess the extracerebral contamination.

A first aspect of interest of our study was directed toward an assessment of the influence of the CSF by comparing simulations performed on a brain area comprising sulci filled with CSF (see Fig. 1) with simulations on another area with a small volume of CSF. A second major focus was related to the influence of the relative blood content in the various transilluminated tissues, because the first place the OD signal is obtained from is the intravascular space where the change of the blood content over time is highest. With respect to the clinical application of NIRS ICG dye dilution, the dependency of the baseline signal on the blood volumina within the different tissues of the head is a key characteristic because ICG is confined to intravascular spaces. Although the baseline signal measurement is not of further clinical use, this dependency can be used to estimate how large the time-varying, useful OD signal will be when an injected ICG bolus replaces blood partially. The resulting blood-ICG intermix causes a transient change of absorption within the tissues of the observed optical segment. This follows from the assumption that the probability for an interaction of a photon with the blood-ICG intermix to occur increases with increasing relative blood volume (rel. BV) of the involved tissues. The rel. BV for each tissue was given per 100 cm^3 of tissue and assumed to vary between the tissue types according to published data.

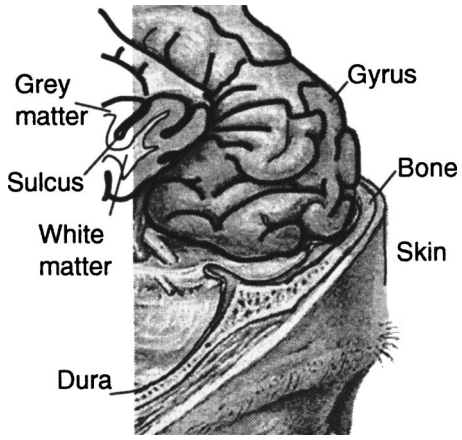

Fig. 1 Human forebrain folded and structured in gyri and sulci. The different layers shown in the figure are the scalp, the skull, the grey matter, and the white matter. The CSF (not highlighted in the figure) surrounds the brain, filling the sulci and the interspace to the dura.

Apart from arterial pulsation, which is the major origin of the OD signal, the rel. BV may furthermore change markedly within time intervals relevant for measurements (sometimes within seconds). A change in rel. BV yields a baseline shift in a typical NIRS measurement. If the change is sufficiently rapid (seconds), it is amenable to an evaluation. Wolf et al.,[35] for example used the finding that the OD signal varies synchronously with ventilation to determine venous oxygenation in neonates.

In this study, the rel. BV was understood as a mean value, averaged over arterial pulsations of blood contained within a unit volume of tissue. In the literature, the rel. BV of the gray and white matter is often denoted as CBV. The CBV within the brain tissues includes the arterial, capillary, and venous blood components of the cerebral vessel system[36,37] whereby 70 to 80% of the CBV is contained within the venous vessels.[38]

In earlier days, no direct attempts were made to quantify the CBV, although the CBV was estimated to change in a

power-law relationship: $CBV = 0.8 \times CBF^{0.38}$ with the CBF, as found by Grubb.[39] More recently, the CBV, respectively its changes, were determined directly using various methods. The work of Ito[40] documented the overall change of CBV, while his newer studies[37] focused on the change in the arterial component of the CBV during hypercapnia and hypocapnia, using positron emission tomography (PET) with H(2)(15)O and (11)CO. Other PET studies[41] showed an increase of the CBV in relation to sodium nitroprusside in an anesthetized baboon. In another approach, the regional cerebrovascular response, including arterial and venous change of CBV, to sympathoexcitatory reflexes was evaluated with contrast-enhanced computer tomography (CT).[36] Additionally, a functional MRI was used to measure the change in CBV with high temporal resolution in relation to visual stimulation[42] with a ΔCBV of $27 \pm 4\%$.

For the MC simulations absorption and scattering properties of the various tissues of interest here were taken from the literature. Because published values are mostly based on measurements performed on excised tissue, however, it is to be assumed that the (unknown) blood content associated with these values is generally low. It is not unreasonable to hypothesize that the enormous spread of the published data can at least partially be attributed to differences in blood content. Accordingly, a comparison of the baseline results obtained with selected tissues assumed hypothetically to have a low and homogeneously distributed blood content with three different cases of higher blood content was made ("standard" case, furthermore, "below average," and "best" case). These simulations served to estimate the highest possible baseline and subsequently the highest possible OD signal that can be expected to originate from each tissue. The passage of the blood-ICG intermix increases the effect further according to the rel. BV.

2 Materials and Methods

2.1 *Anatomical Model and Material Matrix*

MRI scans were performed on a Philip's Intera 3T whole-body unit equipped with a transmit-receive body coil and a commercial eight-element head coil array (MRI Devices Corporation, Waukesha, Wisconsin). T2-weighted anatomical images were obtained with a turbo spin echo sequence (TE/TR=80/4000 ms) from 155 slices covering the whole brain as shown in the sagittal section in Fig. 2 with a spatial resolution of $0.8 \times 0.8 \times 0.8$ mm. T1-weighted anatomical images were acquired with a 3D T1-weighted gradient echo sequence (TE/TR=2.3/20 ms) with the same positioning and geometry. Enhancement of brain vascular structures was achieved with a 3D inflow-weighted gradient echo sequence with TE/TR=1.88/21 ms and maximum intensity projection reconstruction. The MRI results of the three complete scans were stored in three separate 3D matrices with each having a resolution of 2^{16} gray scales.

We processed the MRI data of the three T1/T2 value matrices with a feature and structure matching algorithm to eliminate artifacts due to movements of the healthy volunteer, a 30-year-old male, during the three 20-min measurement times. The perceived matching accuracy of the three MRI data matrices was at 0.5 mm within the range of the image resolution. The result was stored in one 3D data set of $512 \times 512 \times 100 = 26\,214\,400$ voxels. Next, we selected one slice of the 3D MRI data set (Fig. 3) and defined thresholds dependent on the MRI histogram. These thresholds were used to segment the MRI data set into the different tissue types, namely the scalp, the skull, the CSF, and the gray and the white matter. We also included the air around the head of the healthy volunteer. The result of this segmentation process for the white matter is shown for the selected MRI slice in Fig. 3(b) in comparison with the unsegmented MRI of the same slice [Fig. 3(a)].

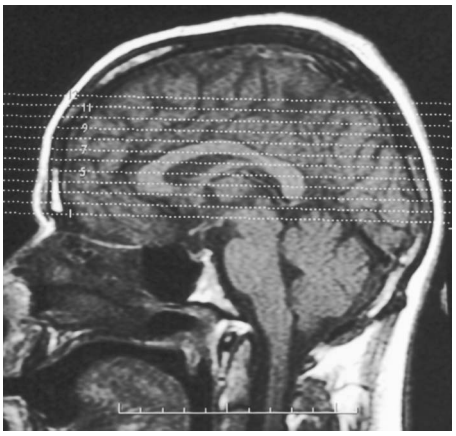

Fig. 2 The 3D MRI data of the head were taken in 155 slices covering the whole brain, where 12 of them are shown in the sagittal section to mark the range of measurement.

Finally, we obtained a 3D matrix (hereafter called material matrix) having the size of $512 \times 512 \times 100$ voxels containing the identification numbers of the different tissues of the brain. The identification was used to assign tissue-specific absorption and scattering coefficients (scalp, skull, CSF, gray and white matter) to each voxel.

We intended in particular to analyze the spatial sensitivity profile, which is defined by the density distribution of those emitted photons that reach the receiver, in the case where the examined human forebrain region contained a deep sulcus near the temple (Fig. 1) filled with a high volume of CSF. These results were then compared with the photon density distribution within a region 1.5 cm further to the sagittal line of the head, which contained only a small sulcus filled with

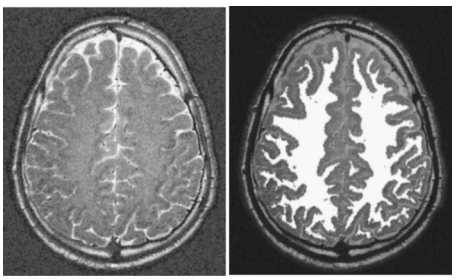

Fig. 3 (a) MRI slice after the matching of the three MRI data sets with the three different T1/T2 values. (b) Within the same MRI slice, one result of the segmentation process is shown using the example of the white matter.

Table 1 Optical attributes of excised human tissues under physiological condition as taken from the literature.

Tissue	λ (nm)	μ_a (1/mm)	μ_s (1/mm)	$\mu_s'=\mu_s[1-g(\lambda)]$ (1/mm)	g (1)	Reference
Muscle	515	1.12	53.0	–	–	56
Skin	633	0.27	18.7	3.55	0.81	45
Scalp	800	0.018	–	1.9	–	57
Skull	800	0.016	–	1.6	0.9	57
CSF	800	0.001	–	0.01	–	29
Gray matter	800	0.036	–	2.2	0.82	43 and 57
White matter	800	0.014	–	9.1	0.957	43 and 57

less CSF. To this end, the CSF volumina were calculated from the segmented MRI data. For both configurations that were simulated, a region of interest was defined containing 10 slices and covering the area spanned by the largest emitter-detector distance under consideration, which was $d_3=4.5$ cm. For both configurations, the number of pixels representing CSF were counted. The region with the high volume of CSF (slice 6 in Fig. 1) contained approximately $CSF=1.7$ ml, while the region with the small amount of CSF (slice 8 in Fig. 1) included approximately $CSF=0.7$ ml. The CSF volume ratio between the region with a high amount of CSF to the one with a small amount was thus 2.4. The simulations were carried out for emitter-detector distances of $d_1=2$ cm, $d_2=3$ cm, and $d_3=4.5$ cm, respectively.

2.2 *MC Simulation*

The NIRS measurement corresponds to the measurement of the time-varying intensity of a stream of photons, assumed to propagate in a stochastic fashion in the tissue. When a photon is scattered elastically in an optically dense material where the scattering centers are large compared to the wavelength, such as is the case in biological tissue, the scattering is of the Mie type. Elastic scattering is characterized by the fact that the photon energy does not change; in the case of Mie elastic scattering, furthermore, the scattering is highly oriented in a forward direction. Accordingly, an anisotropic scattering scheme was used for the simulations.

For the MC procedure, based on the anisotropic modeling approach of Prahl,[34] we simulated the path of individual photons whereby each photon started at the emitter and was allowed to interact with the different tissues. This interaction included elastic scattering and redirection (Sec. 2.2.1) or absorption (Sec. 2.2.2) of a photon. At boundaries, furthermore, internal reflection may occur according to the optical densities (Sec. 2.2.3). Those photons that reached the detector were considered to be as "successful" and were sampled.

During the propagation, we let each photon travel a given distance Δl while it was checked at each step whether the photon had passed the border between two materials or if the photon had been scattered or absorbed. The step-size Δl was chosen to be 0.01 mm, which was sufficiently small to ascertain that a photon could not pass through different materials without taking into account the associated changes in the absorption and scattering coefficients.

2.2.1 *Scattering*

Within the framework of anisotropic scattering, the scattering coefficient μ_s is used to describe the statistical nature of the scattering process. The unit is given as $1/mm$, and the probability for the occurrence of a scattering process over the distance ds is given by

$$p(\text{scattering in } ds) = \mu_s ds. \tag{1}$$

In a dense medium, the values of μ_s are often found to be quite high such that they are difficult to measure. Instead, the reduced or transport scattering coefficient, μ_s', is usually documented in the literature because it is less critical to determine and because it is derived from the diffusion approximation. The relationship between the scatter coefficient μ_s and the reduced scatter coefficient μ_s' is given by $\mu_s'=\mu_s[1-g(\lambda)]$.[43] Thereby, the anisotropy factor $g(\lambda)=\langle\cos\theta\rangle$ describes the mean scattering-induced deviation θ from the forward direction, while it is independent from the azimuthal orientation (transverse anisotropy). It depends in general on the wavelength, which is constant in our case. A typical value for biological tissue is $g=0.9$ as can be seen in Table 1. This implies that the light is scattered mainly in a forward direction with a small diversion.

The scattering angle θ was assumed to change with the material. According to Henyey and Greenstein,[44] the probability distribution for the interaction between biological tissue and near-infrared light[45] can be given as follows:

$$p(\cos\theta) = \frac{1-g^2}{2(1+g^2-2g\cos\theta)^{3/2}}. \tag{2}$$

The anisotropy factors used in our MC simulation are given for the different tissues in Table 2 (see Sec. 2.2.3). In the actual implementation, the stochastic nature of the propagation was taken into account by choosing for each photon the scattering angle from a random number ξ, where $\xi\in[0,1)$. θ is then given as follows:[34]

Table 2 Optical attributes of human tissues as used for the MC simulation. The optical properties of the CSF are not based on experimental data, instead, the coefficients are chosen in relation to previously performed simulations by Okada (Ref. 29).

Tissue	λ (nm)	μ_a (1/mm)	μ_s (1/mm)	μ_s' (1/mm)	g (1)	Refractive index (1)
Air around head	800	2.0	5.0	0.1	1	1
Scalp	800	0.018	10.0	1.8	0.81	1.3
Skull	800	0.016	17.0	1.6	0.91	1.3
CSF	800	0.001	2.0	0.02	0.99	1
Gray matter	800	0.036	37.0	2.2	0.97	1.3
White matter	800	0.014	53.0	9.1	0.82[a]	1.3

[a]Reference 43.

$$\theta = \arccos\left\{\frac{1}{2g}\left[1+g^2-\left(\frac{1-g^2}{1-g+2g\xi}\right)^2\right]\right\} \text{ for } g \neq 0,$$

$$\theta = \arccos(2\xi - 1) \text{ for } g = 0. \quad (3)$$

In agreement with transverse anisotropy, azimuthal scattering was assumed to be isotropic, such that the probability distribution for ψ was considered uniform

$$p(\psi) = \frac{1}{2\pi} \quad (4)$$

such that $\psi = 2\pi\zeta$ with the random number $\zeta \in [0,1)$.

2.2.2 *Absorption*

The probability of absorption along a path of length ds is calculated as

$$p(\text{absorption in } ds) = \mu_a ds. \quad (5)$$

If a photon is absorbed, it is discarded from the simulation. Because probabilities are smaller than 1, care was taken that the incremental pathlength was sufficiently small (in addition to geometrical constraints given by the anatomical details) that the sum of the scattering and absorption probability did not violate this condition.

2.2.3 *Optical coefficients and internal reflection*

The optical attributes of each voxel were given by a pair of values for μ_a and $\mu_s = \mu_s' 1/[1-g(\lambda)]$, which were derived from the literature. It is found that the published values for both coefficients μ_a and μ_s' differ widely, which can be attributed in part to difficulties in isolating the relevant tissue within the living organism. When the measurements were performed under excised conditions, furthermore, the results show changes in the optical attributes with increasing duration from the time of excision. Of particular importance for our work is the circumstance that the blood content of the tissue at the time of measurement is not known (or not reported); yet this parameter influences the optical properties of a biological tissue decisively. Table 1 contains a collection of literature values and documents the variations that were found between the different materials. Apart from the absorption coefficients and the scattering coefficients, the table also contains the values of the anisotropy factor g.

We performed our simulations using the set of optical properties μ_a, μ_s, g and the refractive index for the different tissues of the adult head as listed in Table 2, provided by van der Zee[43] and Okada[26] and also used by Fukui.[31]

Internal reflection was taken into account by applying Fresnel's equation and Snell's law whenever a photon crossed the borderline from one tissue to another and having a different index of refraction.

2.3 *The Implementation of the MC Simulation*

The incremental step-size was chosen as 0.01 mm, such that the passage of a photon through more than one material boundary in one step was avoided. This value was a compromise in that the limitation given by the maximal reciprocal values of μ_a and μ_s, which are in the range of 0.002 to 0.2 mm had to be observed in addition (Table 2), while the time necessary for the computation was kept as small as possible. For the rest, the general procedure followed the one published by Prahl.[34]

The lifetime of a photon includes the three phases "birth," the repeated decision process, and "death."

2.3.1 *Birth*

The random generator created a photon at the surface of the emitter optode. The photon obtained an initial direction of flight within the defined angle of the light beam of the optode.

2.3.2 *Decision process*

When a photon had moved a step of length Δl in its initial direction, a decision was made with respect to the further motion of the photon. The current coordinates of the photon were related to the material matrix to determine the probability of absorption using μ_a from the lookup table. If absorption had not occurred, the probability for scattering was evaluated and a new direction of the photon was determined based on the random numbers ξ and ζ according to Eqs. (3) and (4) to

Table 3 Calculated photon density distribution of the different brain tissues for $d_1=2$ cm, $d_2=3$ cm, and $d_3=4.5$ cm at brain regions with high (1.7-ml CSF) and low volumes of CSF (0.7-ml CSF) in the surrounding. +: The rel. BV content of the sample probes with which the optical parameters were determined are assumed to be very low and set to one (normalized unit) for later weighting purposes for all tissues except for the CSF. CSF of a healthy person does not contain blood at all.

Tissue	Rel. BV in sample	Low volume of CSF			High volume of CSF		
		2 cm	3 cm	4.5 cm	2 cm	3 cm	4.5 cm
Scalp	+1.0	53%	50%	41%	64%	56%	40%
Skull	+1.0	47%	37%	38%	33%	36%	32%
CSF	+0	0%	3%	5%	1%	2%	6%
Gray matter	+1.0	0%	6%	11%	1%	4%	17%
White matter	+1.0	0%	4%	5%	1%	2%	5%

get ψ and θ. Backscattering was taken into account, when the photon had passed a tissue boundary (see Sec. 2.2.3).

2.3.3 *Death*

The stepwise procedure was repeated until the photon was detected successfully or it "died." A photon was considered successful when it crossed the defined detector plane in the distance of $d_1=2$ cm, $d_2=3$ cm, and $d_3=4.5$ cm, respectively, with an entry angle that was within the range of the defined angle of acceptance ($\beta=90$ deg) of the optode. The photon was registered and the path was stored. In turn, death occurred whenever a photon was absorbed (Sec. 2.3.2), exceeded a specified distance from the detector surface, or moved outside the head into air (reentry could be excluded because of the convex shape of the head). The paths of dead photons were discarded.

2.4 *Evaluation*

First, two series of MC simulations were performed, one modeling a configuration with a low CSF volume in the tissue and a second set highlighting a situation with a higher CSF volume (see Table 3). Each series comprised the emitter-detector distances $d_1=2$ cm, $d_2=3$ cm, and $d_3=4.5$ cm, respectively, and every simulation was done with 30×10^6 photons in total, subdivided into three portions of 10×10^6 photons each. After each run, the number of successful paths as well as the differential pathlength factor (DPF) value along with the photon density distribution within the different tissue types were recorded. Care was taken that the standard deviation was less than 3% in all cases.

For simplicity and completeness, the simulations included the absorption processes, although approaches have been presented where the photon trajectories are determined in the absence of absorption and then reweighted.[46] For short distances, $d_1=2$ cm, the processing time was short enough to accept the waste of absorbed photons. For the longer emitter-detector distances, we included a reduction factor to minimize the effect of absorption. However, the chosen reduction factor k for μ_a influences the result of the MC simulation in that for $0<k<1$, paths with a short pathlength s^* are favored. In the case $k=0$, no absorption takes place. For such a case, the successful paths have to be reweighted as described in other implementations.[46] The associated procedure was as follows:

$$p_{Success}(s^*)=\exp[-s^*(1-k)] \tag{6}$$

with

$$s^*=\int_0^d \mu_a ds. \tag{7}$$

This lowered the number of successful paths between the emitter and the detector according to the effect of absorption.

Another side effect of reducing μ_a by a factor k consisted of allowing photons to stay alive even when they had moved away so far that they never would reach the detector surface any more. As a consequence, processing time increased. To minimize this problem, we ignored photons that had traveled a total path length that was longer than a specified distance from the detector surface (50 times the emitter-detector distance).

For the compilation of the photon density distribution, each successful photon path was scrutinized stepwise according to the tissue that had been passed. This distribution was assumed to represent a direct measure for the baseline and the OD signal to be expected under equivalent condition. To this end, the number of path segments in each tissue was related to the total number of segments to yield a relative fraction (%). Both baseline and OD signal were assumed to exhibit the same dependence on the local photon density.

2.5 *Influence of Tissue Blood Content*

In the presented approach, the 3D anatomical structure of the brain region was taken into account in detail, while the primary blood content within the different tissues was not considered. At this time, it is not possible to visualize all small blood vessels within the cerebral tissue and simulate the dynamics of the blood flow within the cerebral vessels. As will be mentioned later in this section, blood and blood-ICG inter-

Table 4 Standard case: Calculated photon density distributions of Table 3 were weighted with the rel. BV within the tissue for $d_1=2$ cm, $d_2=3$ cm, and $d_3=4.5$ cm at brain regions with high and low volumes of CSF in the surrounding. ♦: The values for the rel. BV for scalp and scull were calculated based on CBF values published by Xu (Ref. 48) and Zhu (Ref. 49). ◇: The CBV for white and gray matter were published by Leenders (Ref. 47) in 1990. ☆: For healthy volunteers, CSF does not contain blood and therefore it does not contribute to changes in the baseline of the OD signal.

Tissue	Rel. BV for standard case	Low volume of CSF			High volume of CSF		
		2 cm	3 cm	4.5 cm	2 cm	3 cm	4.5 cm
Scalp	♦1.0	69%	45%	30%	72%	56%	25%
Skull	♦0.5	31%	17%	14%	19%	18%	10%
CSF	☆0	0%	0%	0%	0%	0%	0%
Gray Matter	◇5.2	0%	28%	45%	6%	21%	56%
White matter	◇2.7	0%	10%	11%	3%	5%	9%

mix have different passage velocities in the intracerebral and extracerebral tissues, whereby ICG does not pass the capillary walls.

The MC simulations described so far included optical characteristics of the different tissues as reported in the literature (baseline conditions). As the associated values were determined by using tissue samples where the blood content was not specified or unknown, it was only possible to make hypothetical assumptions with respect to the effects on the OD signal associated with changes in the blood content of the various tissues. The simulations outlined in the following were nevertheless considered useful, because they allowed us to assess the clinical significance of the NIRS ICG dye dilution measurement method.

Three theoretical cases with different sets of rel. BV contents were considered: a "standard," a "below average," and a "best" case scenario (Tables 4–6). The respective rel. BV values were chosen according to literature data. ICG dye was at first not taken into account in these simulations. In a further step, the case of NIRS in combination with ICG dye dilution was approximated. After bolus injection, the rel. BV in the tissues will rapidly be replaced with the blood-ICG dye intermix causing a large jump of the OD signal due to the high absorption of ICG. Yet, the measured slope of this signal cannot be attributed to a specific tissue in a straightforward manner because the ICG reaches all tissues involved in the measurement but the mean transit times mtt_{ICG} are different. Accordingly, the possible effect of the first passage of the blood-ICG dye passage within the observed optical segment was assessed by consideration of different exchange fractions Δ of the rel. BV (Table 7) containing the blood-ICG intermix.

Yet another aspect is of interest. Baseline conditions associated with a given rel. BV cannot be quantified as long as these conditions are strictly constant. Under certain clinical circumstances, however, such as in neurointensive care, rela-

Table 5 Below average case: Calculated photon density distributions of Table 3 are weighted with the rel. BV within the tissue for $d_1=2$ cm, $d_2=3$ cm, and $d_3=4.5$ cm at brain regions with high and low volumes of CSF in the surrounding areas. For the below average case, the rel. BV values, given in Table 4, were reduced by 5% for the extracerebral tissues of scalp and skull (♦), while the rel. BV for the cerebral tissue of gray and white matter (◇) were reduced by 15%. ☆: For healthy volunteers, CSF does not contain blood and therefore it does not contribute to changes in the baseline of the OD signal.

Tissue	Rel. BV for below average case	Low volume of CSF			High volume of CSF		
		2 cm	3 cm	4.5 cm	2 cm	3 cm	4.5 cm
Scalp	♦1.0 −5% = 0.95	69%	47%	33%	73%	57%	25%
Skull	♦0.5 −5% = 0.475	31%	18%	15%	19%	18%	16%
CSF	☆0	0%	0%	0%	0%	0%	0%
Gray matter	◇5.2 −15% = 4.42	0%	26%	42%	5%	19%	51%
White matter	◇2.7 −15% = 2.295	0%	9%	10%	3%	5%	8%

Table 6 Best case scenario: Calculated photon density distributions of Table 3 weighted with the change in the relative blood volume within the tissue for $d_1=2$ cm, $d_2=3$ cm, and $d_3=4.5$ cm at brain regions with high and low volumes of CSF in the surrounding. For the best case, the rel. BV values, given in Table 4, were increased by 5% for the extracerebral tissues of scalp and skull (♦), while the rel. BV for the cerebral tissue of gray and white matter (◇) were enlarged by 15%. ☆: For healthy volunteers, CSF does not contain blood and therefore it does not contribute to changes in the baseline of the OD signal.

Tissue	Rel. BV for best case	Low volume of CSF			High volume of CSF		
		2 cm	3 cm	4.5 cm	2 cm	3 cm	4.5 cm
Scalp	♦ 1.0+5%=1.05	69%	44%	30%	72%	54%	24%
Skull	♦ 0.5+5%=0.525	31%	16%	13%	18%	18%	9%
CSF	☆0	0%	0%	0%	0%	0%	0%
Gray matter	◇ 5.2+15%=5.98	0%	30%	46%	7%	22%	58%
White matter	◇ 2.7+15%=3.105	0%	10%	11%	3%	6%	9%

tively slow (in comparison to the heart beat) and small changes of the baseline conditions themselves, given by the primary rel. BV are observed. Likewise, a signal that varies synchronously with the breathing cycle can be isolated (e.g., Fig. 4). As such changes may be significant and important clinically, an analysis of the dependence of the measured values of the rel. BV of the various tissues involved is of relevance.

As a positive circumstance in view of clinical applications, the rel. BV for gray and white matter is higher than for the scalp and skull. Leenders[47] estimated the CBV, here used as the rel. BV and measured in ml/100 g, for gray matter to be 5.2 and for white matter to be 2.7, respectively. The rel. BV factors for scalp and skull, in turn, were calculated from values of the CBF values published by Xu Zhu,[48,49] where the CBF is given with 50.2 for the brain, 0 (Ref. 48) or 1.8 (Ref. 49) for the bone and 2.0 for the scalp, measured in ml/min $\times$100 g. These values have been considered as the standard case in the following.

Based on these findings, the assumptions made for the below average and the best cases were based on the following further considerations: First, the change of rel. BV for the brain tissue is related to the change in CBV, which has been estimated to vary in a power-law relationship with the CBF ($CBV=0.8\times CBF^{0.38}$, Grubb[39]), implying that 15 to 20% of the relative blood content is exchanged per unit of time. Functional MRI studies with high temporal resolution in relation to visual stimulation,[42] yielded a ΔCBV of 27±4%. Other groups reported a CBV increase of 10±13% for optic flicker simulation with 2-Hz and 21±5% for 8-Hz stimulation frequencies.[50] Average CBV increases for humans have been

Table 7 Influence of the exchange fraction Δ of the rel. BV content, while NIRS ICG dye dilution is performed and a blood-ICG intermix passes the optical segment: Calculated photon density distributions of Table 3 were weighted with the exchange fraction Δ of the rel. BV within the tissue for $d_1=2$ cm, $d_2=3$ cm, and $d_3=4.5$ cm at brain regions with high and low volumes of CSF in the surrounding. The values for the rel. BV are taken from Table 4. The exchange fraction Δ of the rel. BV values for the extracerebral tissues of scalp and skull (♦) were assumed to be on the order of 10%, while the exchange fraction of the rel. BV for the cerebral tissue of gray and white matter (◇) were assumed to be on the order of 30%. ☆: For healthy volunteers, CSF does not contain blood and therefore it does not contribute to changes of the OD signal.

Tissue	Exchange fraction Δ rel. BV	Low volume of CSF			High volume of CSF		
		2 cm	3 cm	4.5 cm	2 cm	3 cm	4.5 cm
Scalp	♦ 1.0×0.1=0.1	70%	26%	14%	61%	37%	11%
Skull	♦ 0.5×0.1=0.05	30%	10%	7%	16%	12%	4%
CSF	☆0	0%	0%	0%	0%	0%	0%
Gray matter	◇ 5.2×0.3=1.56	0%	48%	64%	15%	41%	74%
White matter	◇ 2.7×0.3=0.81	0%	16%	15%	8%	10%	11%

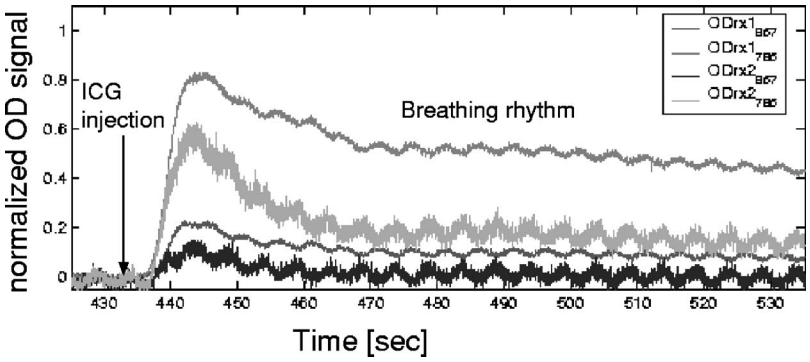

Fig. 4 Presented are the monitored OD signal of the two receivers (rx1 and rx2) used for the bilateral NIRS setup applied on a patient, each for the wavelengths of 857 and 785 nm. The time frame is chosen to show the changes in the monitored ODs after an ICG dys dilution injection has been applied on the patient who is artificially ventilated with an inspiratory pressure of 25 mbar and an expiratory pressure of 10 mbar. The strong rise in the OD signal is caused by the high absorption coefficient of the injected ICG dye, while the small waves on top of the slopes axe showing the variation of the blood content in the monitored optical segments in relation to the different inspiratory pressure.

measured in the range of $32\pm10\%$,[51] $10.9\pm2.5\%$,[52] $23.5\pm14.6\%$,[53] and $28\pm7\%$[54] in bolus tracking MRI experiments. Based on these reported data, we assumed a change in the rel. BV for gray and white matter of 30% as representative to estimate the influence on the monitored OD signals during NIRS with ICG dye dilution. That the change in the rel. BV can be monitored with NIRS accompanied by ICG dye dilution is shown in the following case (Fig. 4), where a patient was mechanically ventilated with an inspiratory pressure of 25 mbar and an expiratory pressure of 10 mbar.

From our unpublished results for NIRS ICG dye dilution measurements, we perceived transit times of ICG (mtt_{ICG}) in the range 5 to 12 sec for the brain tissue. The mtt_{ICG} for the scalp was measured to be approximately 20 sec on a patient with a brain herniation, where the interruption of the CBF circulation could be documented with a transcranial Doppler measurement. Based on the relationship $CBF=CBV/mtt$, we estimated as representative factors the ones presented in Tables 5 and 6. The change in rel. BV in the extracerebral tissue was assumed to be smaller than in the cerebral tissue, due to the fact that the blood flow is smaller and slower. The change of rel. BV in extracerebral tissue was therefore estimated to be on the order of 10%. In healthy persons, the CSF does not contain blood, and based on this circumstance, it was not assumed to cause changes in the OD signals.

To analyze the influence of the rel. BV content on the baseline signals, the above mentioned changes in rel. BV values (30% corresponding to ±15% and 10% corresponding to ±5%, respectively) were used to reweight the MC simulation results of the spatial photon density distribution within the different tissues.

In the below average scenario, we hypothesized that the results of the primary simulations could be weighted with the rel. BV contents as mentioned above: A reduction of 5% for scalp and skull and of 15% for gray and white matter was assumed. In turn, for the best case scenario, the rel. BV contents were increased by 5% for scalp and skull and by 15% for the gray and white matter. The results of these weightings are given in Tables 5 and 6.

In order to model the passage of an ICG bolus through the observed optical segment hypothetically, the exchange fractions of the rel. BV, Δ (exchange of intravascular volume per unit of time due to blood flow) were assumed as 10% (relatively slow blood perfusion) for scalp and skull, while those for gray and white matter were set to 30% (high blood perfusion). Only in this scenario, which involves the application of ICG, can the maximal possible change in the absorption be monitored: As long as no ICG dye is present, the exchange Δ of the rel. BV does not manifest itself because there is no change in the absorption coefficient, under the assumption that the blood content itself is constant.

Finally, the DPF was determined from the step-size Δl and the number of steps n the photon needed to pass from the emitter to the detector according to

$$DPF = \frac{n\Delta l}{d}. \tag{8}$$

Because the ICG concentration is strongly changing between the time of injection (bolus) and the first and second passage of the optically observed brain segment and further decreases according to the clearance rate of the liver, which under normal conditions, causes ICG to disappear within 15 to 20 min after injection, the change of the DPF due to altered paths of the photons was not considered.

3 Result

A first simulation series was devoted to three different emitter-detector distances applied to the human forebrain, whereby the region of interest was near the temple (near slice 8 in Fig. 1), an area that includes a deep sulcus with a high amount of CSF. Further simulations were performed 1.5 cm closer to the sagittal line of the head (approximately slice 6 in Fig. 1). This region contains less CSF (volume). The MC simulations for the smallest emitter-detector distance of $d_1 = 2$ cm were made with no reduction factor (i.e., $k=1$) in order to verify the influence of the absorption factor μ_a. For the arrangement with an interoptode distance of $d_2=3$ cm, the reduction factor for the absorption was set to $k=0.1$. In case of the distance of $d_3=4.5$ cm, a reduction factor of $k=0.01$

was used. For all simulations, the opening angle of the light beam of the emitter optode was specified to be $\alpha=45$ deg.

The results of the simulations pertaining to the region with a low CSF volume are shown in Fig. 5, while those relating to the region with a deep sulcus filled with a large volume of CSF are shown in Fig. 6.

3.1 *Photon Density Distribution within the Tissues*

The successful paths of the photons were analyzed to extract information with respect to the tissues that were traversed and to the spatial photon density distribution in each material. In Table 3, the relative photon density distributions are listed for the tissues of the scalp, skull, CSF, gray matter and white matter. A distinction was thereby made between the emitter-detector pair at positions with high and low CSF volume in the optically observed areas, respectively.

There is a relatively small difference in the overall photon density distribution between the three examined emitter-detector pair positions. With a emitter-detector spacing $d_1=2$ cm, however, simulated photons travel almost entirely through the scalp and skull only, while for $d_2=3$ cm, 6 to 10% and for $d_3=4.5$ cm approximately 16 to 22% of the photons also pervade the brain. As expected, with increasing emitter-detector distance, the photon density in the gray and white matter increase. Yet, the simulated photon density distributions are still low, which implies that even in the best case, only 22% of the OD signal is obtained from gray and white matter, while the rest of the signal is dominated by extracerebral contamination.

These results (Table 3, baseline conditions) describe the situation where the observed optical segment is associated with unknown, presumably very low rel. BV content within the different tissues. The weighted results, taking the blood content for standard, below average, and best case scenarios into account are given in Tables 4–6, respectively.

The weighted simulation results for the sampled optical segments with a low volume of CSF show that for the average case 5 to 51% and for the best case 7 to 58% of the photon density distribution can be expected to derive from the gray matter, depending on the chosen emitter-detector distance. Furthermore, 3 to 10%, or 3 to 11%, respectively, of the photon density distribution is postulated to be located in the white matter for an emitter-detector spacing between $d_2=3$ cm to $d_3=4.5$ cm. For the distance of $d_1=2$ cm, the white matter is hardly traversed. This allows us to conclude that the probability that a photon passes through the brain tissue is given by 0 to 10% for a distance of $d_1=2$ cm for the below average or best case of rel. BV content and up to 53 to 68% for a distance of $d_3=4.5$ cm for below average or best case, respectively.

The following results focus on the time point of NIRS extended with ICG dye dilution technique, when the injected ICG dye passes the monitored brain segment. In order to assess the effects of the first passage of the blood-ICG dye intermix in the observed optical segment on the expected change in absorption, the results were weighted with the exchange fraction Δ of the rel. BV (Table 7). The exchange fraction Δ of the rel. BV is, on the one hand, dependent on the rel. BV content itself and, on the other, also larger for the intracerebral tissue than for the extracerebral tissue. The assumption thereby made was that the blood-ICG dye intermix is dominated by ICG (ICG bolus injection), which due to the high absorption coefficient of ICG becomes apparent.

The weighted results indicate that for the first passage of blood-ICG dye intermix, at best, between 64 to 74% of the OD signal is determined by the gray matter of the cerebral cortex for an emitter-detector distance of $d_3=4.5$ cm. Although these results are still strongly dependent on the rel. BV within the tissues and on the exchange fraction Δ of the rel. BV, they allow us to conclude that NIRS together with ICG dye dilution technique can produce useful CBF measurements within neurointensive care monitoring due to the fact that there is a more than 50% possibility that the light is interacting with the ICG dye in the blood vessels of the gray and white matter than with other tissues. Nevertheless, corresponding corrections for the extracerebral contamination still have to be included. The significance of this conclusion has to be relativized insofar as the baseline conditions, in particular the rel. BV at the beginning of the measurement, are not known. Only short-term changes of rel. BV, yet possibly clinically important, can be recorded.

3.2 *Differential Path Length Factor*

We evaluated the DPF on the basis of the simulations of the various configurations. The calculated values, given in Table 8, are compared with DPFs from Okada.[26] As can be seen, our results with a DPF varying between 6.15 and 7.6 depending on the volume of surrounding CSF are similar to those published by Okada,[26] where the DPF is calculated to be 5.9. The value[43] of 5.9 has also been obtained by Okada using MC simulations. Furthermore, Okada examined the change of the DPF in relation to the distance between emitter and detector optodes. He showed that the DPF will decrease when the distance between the optodes is greater than 4.5 cm, while for narrower optode separations, the DPF remains almost constant at 7.5.[26] The explanation he proposed for this effect was that the CSF has an increasing influence on the DPF with increasing distance between the optodes.

Our simulations show that for the low CSF volume case, the DPFs for the emitter-detector distances of $d_1=2$ cm and $d_2=3$ cm were approximately equal. For $d_3=4.5$ cm, the DPF was in turn higher. In contrast, for the simulations with a high volume of CSF in a deep sulcus, the DPF values for $d_1=2$ cm and $d_2=3$ cm were also of the same size, while the DPF for $d_3=4.5$ cm decreased by more than can be explained by the different anatomical structure. Therefore, we note that these results are due to the strong influence of the CSF on the surrounding.

4 Conclusion and Discussion

New neuroprotective treatment options such as hypothermia applied for brain protection after cardiac arrest, severe stroke, or brain injury made it essential to develop new bedside monitoring techniques to detect cerebral ischemic thresholds and to control the effects of treatment. Therefore, the measurement of electrophysiological data, such as electroencephalography or somatosensory, evoked potential, as did the monitoring of cerebral hemodynamics and oxygenation, which are some of the most important issues in neurocritical care.[55]

Since 1993, NIRS ICG dye dilutions[4] has been used for a improved monitoring of cerebral hemodynamics in neuroin-

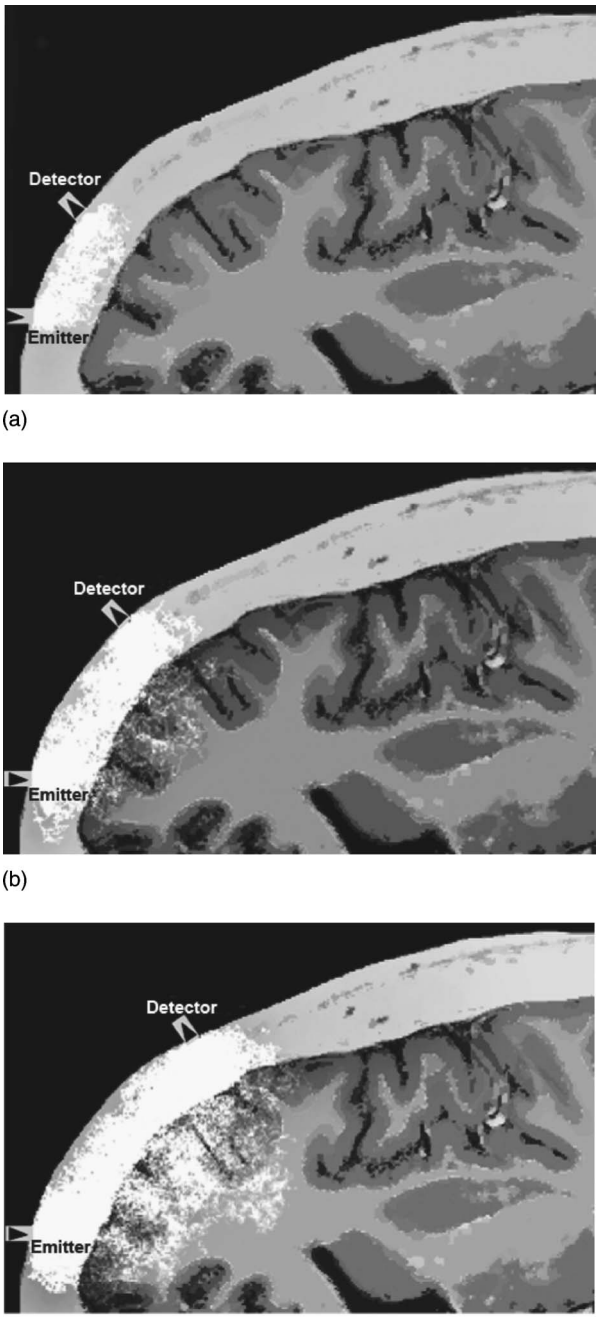

Fig. 5 Simulation of a brain region containing a low volume of CSF. In all three subfigures, the scalp, skull, gray matter, white matter, and CSF are shown in single MRI image. The emitter and detector optode are marked with black arrows on white rectangulars. The arrows mark the direction of the light into the head (emitter) and out of the brain (detector). The successful paths of the MC simulation between emitter and detector are shown overlayed in dark gray. (a) MC simulation result, optode distance $d_1=2$ cm. (b) MC simulation result, optode distance $d_2=3$ cm. (c) MC simulation result, optode distance $d_3=4.5$ cm.

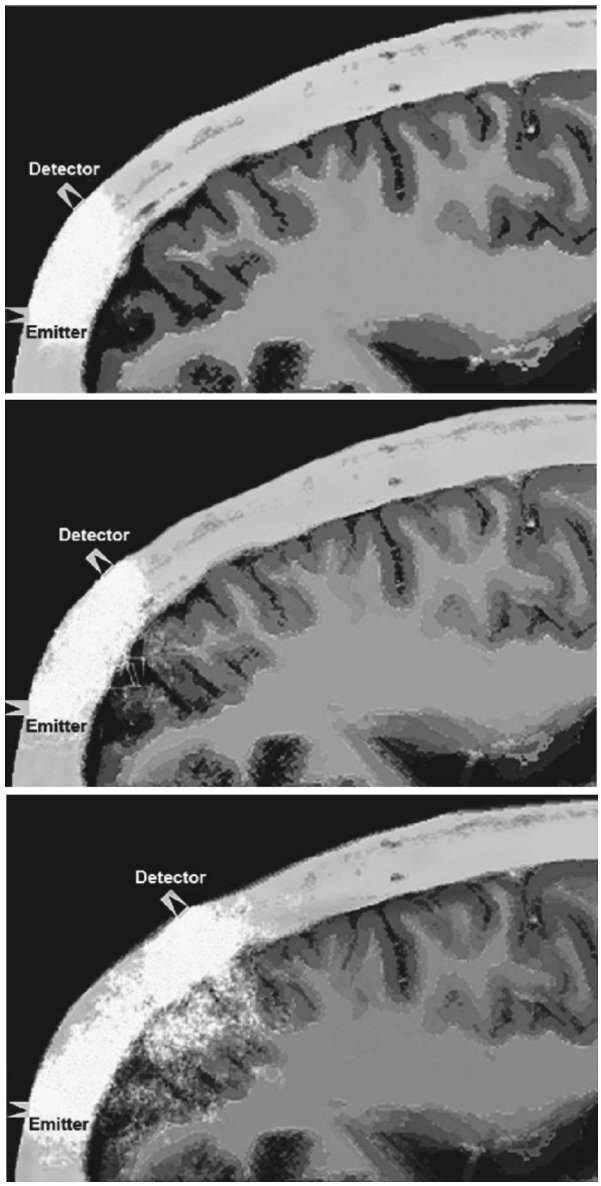

Fig. 6 Simulation of a brain region containing a deep sulcus with a high volume of CSF. Details are the same as in Fig. 5.

tensive care. However, from the first application of the NIRS ICG dye dilution, one of the caveats which has been subjected to discussion is related to the contribution of the extracerebral tissue. A further important aspect is associated with the blood content of the various tissues involved, which may vary considerably (and is unknown in the excised tissues which were used in the published optical data), therefore various scenarios were subjected to a theoretical analysis.

On the basis of MC simulations, the light propagation of NIRS in an anatomical head model was modeled and the statistical photon density distribution in the tissues were estimated. Based on the results, we assume that for a emitter-detector distance of $d_3=4.5$ cm, the contributions from the white and gray matter to the OD signal vary between 16 and 22% (Table 3), that is, the calculated photon density distributions were relatively low with 11 to 17% for the gray matter and 5% for the white matter. We interpret these results as being representative of a scenario with an unknown, but presumably low rel. BV content in the different tissues, in particular in the tissues of clinical interest.

Table 8 Calculated DPF for $d_1=2$ cm, $d_2=3$ cm, and $d_3=4.5$ cm at brain regions with varying volumes of CSF in the surrounding areas. The DPFs obtained from the MC simulation are set in relation to the DPFs of Okada (Ref. 26).

	2 cm	3 cm	4.5 cm
Low volume of CSF	7.15	7.24	7.6
High volume of CSF	6.95	7.05	6.15
Okada[a]	7.5	7.5	5.9

[a]Reference 26.

In order to obtain insight into the influence of the blood content within the different tissues on the baseline signal, standard, below average, or best case conditions with respect to the rel. BV were defined. Accordingly, the calculated photon density distributions were weighted with these rel. BV contents of the tissues, yielding the results of Tables 4–6, respectively. The weighted results for a distance $d_3=4.5$ cm show a range of the baseline signal component obtained from gray and white matter for a low CSF volume of 52 to 57% and for a high volume of CSF of 59 to 67%. This can be summarized in the statement that approximately 50 to 60% of the baseline signal is contributed by the rel. BV contained within the gray and white matter. The weighted results of the three discussed cases of rel. BV in the tissue document that 42 to 58% of the baseline signal is determined by the blood content in the brain vessels in the gray matter for $d_3=4.5$ cm, while 8 to 11% is determined by blood content in the brain vessels in the white matter. It has to be noted, however, that this conclusion is based on a number of hypotheses regarding the rel. BV of the various tissues involved including its influence on the baseline signal. As was explained earlier, the baseline signal is not of interest. For the OD signal, however, it can be assumed that the same dependence on the rel. BV prevails because the OD signal is essentially created in the intravascular space. The same percentages given above also apply approximately for the OD signal.

Additionally, the scenario of NIRS extended with ICG dye dilution has been taken into account. An assumption was made with respect to the influence of the blood-ICG intermix passage, causing a strong change in absorption, for an exchange fraction of $\Delta=30\%$ of the rel. BV content within the intracerebral tissue. One finds that the OD signal is determined under these conditions to an extent of 64 to 74% by the gray matter and between 8 and 16% by the white matter maximally (Table 7). It should be noted, however, that this component of the OD signal is strongly dependent on the baseline of the rel. BV content in the tissues and the exchange fraction. For high rel. BV, the OD signal will be strongly influenced by the blood content in the brain vessels of the white and gray matter, and the exchange fraction will be higher in these tissues and have a stronger contribution to the OD signal when blood-ICG intermix passes the observed optical segment. We therefore conclude that the NIRS measurements in combination with the ICG dye dilution technique through the skull with optodes placed on the scalp contains a significant contribution from brain vessels within the gray and white matter such that mtt_{ICG}, and CBV as well as CBF can be estimated. Yet, under all conditions investigated in the simulation presented in this paper, the extracerebral contamination of the OD signal must still be evaluated and, if necessary, compensated, because even under the most favorable condition, 15% of the OD signal may be derived from extracerebral tissues. This fraction may increase to over 50% under less favorable circumstances.

It was found that the CSF has a significant effect on the OD signals. The reason for this effect derives from the low values of the material coefficients μ_a and μ_s as well as from the index of refraction for CSF. Consequently, the CSF in the interspace between brain and skull functions as a light guide.[20] This light guiding effect can also explain the increase in the photon density distribution through the gray matter with increasing CSF volume. This conclusion is further supported by the calculated DPF values.

The DPF values derived from our simulations for the assumed emitter-detector distances $d_1=2$ cm and $d_2=3$ cm as well as for low and high CSF compartments correspond largely to the DPF values in the literature. We derived a DPF of 6.15 for the case of a high CSF volume over the emitter-detector distance of $d_3=4.5$ cm under baseline conditions (Table 8). This corresponds essentially to the results of MC simulations reported by Okada.[26] In turn, we obtained a DPF of 7.6 for the case of less CSF over the distance of $d_3=4.5$ cm. Okada argued that the DPF is influenced by the CSF and the CSF causes a reduction of the DPF. In the absence of CSF, furthermore, the DPF is the same as for shorter emitter-detector distances. Our results support this argument, even if the DPF of 7.6 is slightly higher compared to the value obtained for shorter distances, but this can be explained by the differences in the anatomical structures, which in our approach are taken into account.

Acknowledgments

This work was supported by the Olga Mayenfisch Foundation and Swiss National Science Foundation (Grant No. 3200B0-102090/1). We would like to thank Conny Schmidt for performing the MRI measurements used for the MC simulation.

References

1. F. F. Jöbsis, "Noninvasive infrared monitoring of cerebral and myocardial oxygen sufficiency and circulatory parameters," *Science* **198**, 1264–1267 (1977).
2. J. S. Wyatt, M. Cope, D. T. Delpy, S. Wray, and E. O. R. Reynolds, "Quantification of cerebral oxygenation and haemodynamics in sick newborn infants by near infrared spectrophotometry," *Lancet* **2**(8515), 1063–1066 (1986).
3. J. S. Wyatt, M. Cope, D. T. Delpy, C. E. Richardson, A. D. Edwards, S. Wray, and E. O. R. Reynolds, "Quantitation of cerebral blood

volume in human infants by near-infrared spectroscopy," *J. Appl. Physiol.* **68**(3), 1086–1091 (l990).
4. I. Roberts, P. Fallon, F. Kirkham, A. Lloyd-Thomas, C. Cooper, R. Maynrad, M. Elliott, and A. D. Edwards, "Estimation of cerebral blood flow with near infrared spectroscopy and indocyanine green," *Lancet* **342**, 1425 (l993).
5. E. Keller, A. Nadler, H. G. Imhof, P. Niederer, P. Roth, and Y. Yonekawa, "New methods for monitoring cerebral oxygenation and hemodynamics in patients with subarachnoid hemorrhage," *Acta Neurochir. Suppl. (Wien)* **82**, 87–92 (2002).
6. E. Keller, A. Nadler, H. Alkadhi, S. S. Kollias, Y. Yonekawa, and P. Niederer, "Noninvasive measurement of regional cerebral blood flow volume by near-infrared spectroscopy and indocyanine green dye dilution," *Neuroimage* **20**(2), 828–839 (2003).
7. T. S. Olsen, B. Larsen, M. Herning, E. B. Skriver, and N. A. Lassen, "Blood flow and vascular reactivity in collaterally perfused brain tissue, evidence of an ischemic penumbra in patients with acute stroke," *Stroke* **14**(3), 332–341 (1983).
8. P. Gideon, B. Sperling, P. Arlien-Soborg, T. S. Olsen, and O. Henriksen, "Long-term follow-up of cerebral infarction patients with proton magnetic resonance spectroscopy," *Stroke* **25**(5), 967–973 (1994).
9. D. E. Saunders, F. A. Howe, A. van den Boogaart, M. A. McLean, J. R. Griffiths, and M. M. Brown, "Continuing ischemic damage after acute middle cerebral artery infarction in humans demonstrated by short-echo proton spectroscopy," *Stroke* **26**(6), 1007–1013 (1995).
10. W. D. Heiss, R. Graf, J. Lottgen, K. Ohta, T. Fujita, R. Wagner, M. Grond, and K. Weinhard, "Repeat positron emission tomographic studies in transient middle cerebral artery occlusion in cats: Residual perfusion and efficacy of postischemic reperfusion," *J. Cereb. Blood Flow Metab.* **17**(4), 388–400 (l997).
11. S. S. Kety and C. F. Schmidt, "The determination of cerebral blood flow in man by the use of nitrous oxide in low concentrations," *Am. J. Physiol.* **143**, 130–136 (l945).
12. W. D. Obrist, H. K. Thompson, H. S. Wang, and W. E. Wikinson, "Regional cerebral blood flow estimated by 133-Xenon inhalation," *Stroke* **6**, 245–256 (1975).
13. P. J. D. Andrews, N. J. Souter, and L. Mascia, "Cerebral blood flow in acute brain injury", in *Yearbook of Intensive Care and Emergency Medicine*, pp. 739–748, Springer, New York (l997).
14. E. Okada, M. Firbank, and D. T. Delpy, "The effect of overlying tissue on the spatial sensitivity profile of near-infrared spectroscopy," *Phys. Med. Biol.* **40**(12), 2093–2108 (1995).
15. T. J. Germon, P. D. Evans, N. J. Barnett, P. Wall, A. R. Manara, and R. J. Nelson, "Cerebral near infrared spectroscopy: Emitter-detector separation must be increased," *Br. J. Anaesth.* **82**(6), 831–837 (1999).
16. S. Hongo, K. Kobayashi, H. Okudera, M. Hokama, and F. Nakagawa, "Noninvasive cerebral optical spectroscopy: Depth-resolved measurements of cerebral hemodynamics using indocyanine green," *Neurol. Res.* **17**, 89–93 (1995).
17. P. Hopton, T. S. Walsh, and A. Lee, "Measurement of cerebral blood volume using near-infrared spectroscopy and indocyanine green elimination," *J. Appl. Physiol.* **87**(5), 1981–1987 (l999).
18. P. W. McCormick, M. Stewart, G. Lewis, M. Dujovny, and J. I. Ausman, "Intracerebral penetration of infrared light. Technical note," *J. Neurosurg.* **76**, 315–318 (l992).
19. H. Owen-Reece, C. E. Elwell, J. S. Wyatt, and D. T. Delpy, "The effect of scalp ischemia on measurement of cerebral blood volume by near-infrared spectroscopy," *Physiol. Meas* **17**, 279–286 (l996).
20. M. Wolf, M. Keel, V. Dietz, K. von Siebenthal, H. U. Bucher, and O. Baenziger, "The influence of a clear layer on near-infrared spectrophotometry measurements using a liquid neonatal head phantom," *Phys. Med. Biol.* **44**, 1743–1753 (1999).
21. S. J. Matcher, C. E. Elwell, C. E. Cooper, D. T. Cope, and M. Delpy, "Absolute quantification methods in tissue," *Proc. SPIE* **2389**, 486–495 (1995).
22. S. Ijichi, T. Kusaka, K. Isobe, K. Okubo, K. Kawada, M. Namba, H. Okada, T. Nishida, T. Imai, and S. Itoh, "Developmental changes of optical properties in neonates determined by near-infrared time-resolved spectroscopy," *Pediatr. Res.* **58**(3), 568–573 (2005).
23. V. Quaresima, M. Ferrari, A. Torricelli, L. Spinelli, A. Pifferi, and R. Cubeddu, "Bilateral prefrontal cortex oxygenation responses to a verbal fluency task: A multichannel time-resolved near-infrared topography study," *J. Biomed. Opt.* **10**(1), 011012 (2005).
24. M. Wolf, U. Wolf, J. H. Choi, R. Gupta, L. P. Safonova, L. A. Paunescu, A. Michalos, and E. Gratton, "Detection of the fast neuronal signal on the motor cortex using functional frequency domain near infrared spectroscopy," *Adv. Exp. Med. Biol.* **510**, 193–197 (2003).
25. M. Firbank, S. R. Arridge, M. Schweiger, and D. T. Delpy, "An investigation of light transport through scattering bodies with non-scattering regions," *Phys. Med. Biol.* **41**, 767–783 (1996).
26. E. Okada and D. T. Delpy, "Effects of scattering of arachnoid trabeculae on light propagation in the adult brain.," *Proc. OSA Biomedical Topical Meeting*, pp. 256–258 (2000).
27. T. Hayashi, Y. Kashio, and E. Okada, "Hybrid Monte Carlo-diffusion method for light propagation in three dimensional models with low scattering layer," *Proc. OSA Biomedical Topical Meeting*, pp. 116–118 (2001).
28. M. Watanabe, K. Honjo, K. Yokoyama, and E. Okada, "Monte Carlo analysis of light propagation in the exposed brain in the wavelength range of 400–950 nm," *Proc. OSA Biomedical Topical Meeting*, pp. 158–160 (2001).
29. E. Okada, M. Firbank, M. Schweiger, S. R. Arridge, and D. T. Delpy, "Theoretical and experimental investigation of near-infrared light propagation in a model of the adult head," *Appl. Opt.* **36**(1), 21–31 (1997).
30. M. Firbank, E. Okada, and D. T. Delpy, "A theoretical study of the signal contribution of regions of the adult head to near-infrared spectroscopy studies of visual evoked responses," *Neuroimage* **8**(1), 69–78 (1998).
31. Y. Fukui, Y. Ajichi, and E. Okada, "Monte Carlo prediction of near-infrared light propagation in realistic adult and neonatal head models.," *Appl. Opt.* **42**(16), 2881–2887 (2003).
32. D. A. Boas, J. P. Culver, J. J. Stott, and A. K. Dunn, "Three dimensional Monte Carlo code for photon migration through complex heterogeneous media including the adult human head," *Opt. Express* **10**(3), 159–170 (1986).
33. G. Strangman, M. A. Franceschini, and D. A. Boas, "Factors affecting the accuracy of near-infrared spectroscopy concentration calculations for focal changes in oxygenation parameters," *Neuroimage* **18**, 865–879 (2003).
34. S. A. Prahl, M. Keijzer, S. L. Jacques, and A. J. Welch, "A Monte Carlo model of light propagation in tissue," in Dosimetry of Laser Radiation in Medicine and Biology, *Proc. SPIE* **IS5**, 102–111 (1989); http://omlc.ogi.edu.
35. M. Wolf, G. Duc, M. Keel, P. Niederer, K. von Siebenthal, and H.-U. Bucher, "Continuous noninvasive measurement of cerebral arterial and venous oxygen saturation at the bedside in mechanically ventilated neonates," *Crit. Care Med.* **25**(9), 1579–1582 (1997).
36. T. W. Wilson, J. K. Shoemaker, R. Kozak, T.-Y. Lee, and A. W. Gelb, "Reflex-mediated reduction in human cerebral blood volume," *J. Cereb. Blood Flow Metab.* **25**, 136–143 (2005).
37. H. Ito, M. Ibaraki, I. Kanno, H. Fukuda, and S. Miura, "Changes in the arterial fraction of human cerebral blood volume during hypercapnia and hypocapna measured by positron emission tomography," *J. Cereb. Blood Flow Metab.* **25**, 852–857 (2005).
38. H. H. Schmidek, L. M. Auer, and J. P. Kapp, "The cerebral venous system," *Neurosurgery* **17**, 663–678 (1985).
39. R. Grubb, M. Phelps, and J. Eichling, "The effects of vascular changes in PaCO2 on cerebral blood volume, blood flow and vascular mean transit time," *Stroke* **5**, 630–639 (1974).
40. H. Ito, I. Kanno, C. Kato, T. Sasaki, K. Ishii, Y. Ouchi, A. Lida, H. Okazawa, K. Hayashida, N. Tsuyuguchi, K. Ishii, Y. Kuwabra, and M. Senda, "Database of normal human cerebral blood flow, cerebral blood volume, cerebral oxygen extraction fraction and cerebral metabolic rate of oxygen measured by positron emission tomography with 15o-labeled carbon dioxide or water, carbon monoxide and oxygen: a multicentre study in Japan," *Eur. J. Nucl. Med. Mol. Imaging* **31**, 635–643 (2004).
41. P. Schumann-Bard, O. Touzani, A. R. Young, J. Toutain, J.-C. Baron, E. T. Mackenzie, and E. A. Schmidt, "Cerebrovascular effects of sodium nitroprusside in the anesthetized baboon: a positron emission tomographic study," *J. Cereb. Blood Flow Metab.* **25**, 535–544 (2005).
42. S. T. Francis, J. A. Pears, S. Butterworth, R. W. Bowtell, and P. A. Gowland, "Measuring the change in CBV upon cortical activation with high temporal resolution using look-locker EPI and gd-DTPA," *Magn. Reson. Med.* **50**, 483–492 (2003).
43. P. van der Zee, M. Essenpreis, and D. T. Delpy, "Optical properties of brain tissue," in *Photon Migration-and-Imaging in Random Media and Tissues*, *Proc. SPIE* **1888**, 454–456 (1993).

44. L. G. Henyey and J. L. Greenstein, "Diffuse radiation in the galaxy," *Astrophys. J.* **93**, 70–83 (1941).
45. S. L. Jacques, C. A. Alter, and S. A. Prahl, "Angular dependence of hene laser light scattering by human dermis," *Lasers Life Sci.* **1**, 309–333 (1987).
46. L. Wang, S. L. Jacques, and L. Zheng, "MCML—Monte Carlo modeling of light transport in multi-layered tissues," *Comput. Methods Programs Biomed.* **47**, 131–146 (1995).
47. K. L. Leenders, D. Perani, A. A. Lammertsma, J. D. Heather, P. Buckingham, M. J. R. Healy, J. M. Gibbs, R. J. S. Wise, J. Hatazawa, S. Herold, R. P. Beaney, D. J. Brooks, T. Spinks, C. Rodes, R. S. J. Frackowiak, and T. Jones, "Cerebral blood flow, blood volume and oxygen utilization normal values and effect of age," *Brain* **113**, 27–47 (1990).
48. X. Xu, P. Tikuisis, and G. Giesbrecht, "A mathematical model for human brain cooling during cold-water near-drowning," *J. Appl. Physiol.* **86**(1), 265–272 (1999).
49. L. Zhu and C. Diao, "Theoretical simulation of temperature distribution in the brain during mild hypothermia treatment for brain injury," *Med. Biol. Eng. Comput.* **39**, 681–687 (2001).
50. H. Ito, K. Takahashi, J. Hatazawa, S. G. Kim, and I. Kanno, "Changes in human regional cerebral blood flow and cerebral blood volume during visual stimulation measured by positron emission tomography," *J. Cereb. Blood Flow Metab.* **21**, 608–612 (2001).
51. J. W. Belliveau, D. N. J. Kennedy, R. C. McKinstry, B. R. Buchbinder, R. M. Weisskoff, M. S. Cohen, J. M. Vevea, T. J. Brady, and B. R. Rosen, "Functional mapping of the human visual cortex by magnetic resonance imaging," *Science* **254**, 716–719 (1991).
52. C. T. Moonen, F. A. Barrios, J. R. Zigun, J. Gillen, G. Liu, G. Sobering, R. Sexton, J. Woo, J. Frank, and D. R. Weinberger, "Functional brain MR imaging based on bolus tracking with a fast $T2^*$-sensitized gradient-echo method," *Magn. Reson. Imaging* **12**, 379–385 (1994).
53. J. Frank, V. Massay, J. Duyn, G. Soberin, F. Barrios, J. Zigun, R. Sexton, P. Kwok, J. Woo, C. Moonen, and D. Weinberger, "Measurement of relative cerebral blood volume changes with visual stimulation by double dose gadopentate dimeglumine enhanced dynamic magnetic resonance imaging," *Invest. Radiol.* **29**, 157–160 (1994).
54. J. Pears, S. Francis, S. Butterworth, R. Bowtell, and P. Gowland, "Investigating the BOLD effect during infusion of gd DTPA using rapid t2 imaging," *Magn. Reson. Med.* **49**, 61–70, (2003).
55. E. Keller, H. Ishihara, A. Nadler, P. Niederer, B. Seifert, Y. Yonekawa, and K. Frei, "Evaluation of brain toxicity following near infrared light exposure after indocyanine green dye injection.," *J. Neurosci. Methods* **117**(1), 23–31 (2002).
56. R. Marchesini, T. Dasdia, E. Melloni, and E. Rocca, "Effect of low-energy laser irradiation on colony formation capability in different human tumor cells *in vitro*," *Lasers Surg. Med.* **9**(1), 59–62 (1989).
57. E. Okada and D. T. Delpy, "Near-infrared light propagation in an adult head model. I. Modeling of low-level scattering in the cerebrospinal fluid layer," *Appl. Opt.* **42**(16), 2906–2914 (2003).